Journal of Materials Chemistry A

PAPER

View Article Online
View Journal

Published on 14 November 2016. Downloaded by SHANDONG UNIVERSITY on 12/12/2016 07:12:12.

Cite this: DOI: 10.1039/c6ta09030c

MOF-derived bi-metal embedded N-doped carbon polyhedral nanocages with enhanced lithium storage†

Man Huang,[ab] Kan Mi,[b] Junhao Zhang,*[a] Huili Liu,[a] Tingting Yu,[a] Aihua Yuan,*[a] Qinghong Kong[c] and Shenglin Xiong*[b]

Received 18th October 2016
Accepted 12th November 2016

DOI: 10.1039/c6ta09030c

www.rsc.org/MaterialsA

To tackle the issue of the low specific capacity (372 mA h g^{-1}) of graphite as the anode material for lithium-ion batteries (LIBs), an effective and controllable strategy was developed to construct porous bimetallic Co/Zn embedded N-doped carbon (Co–Zn/N–C) polyhedral nanocages *via* annealing a ZIF-8@ZIF-67 precursor at 800 °C under Ar atmosphere. The results clearly displayed that metallic Co and Zn particles are uniformly dispersed in the carbon matrix. Porous Co–Zn/N–C polyhedral nanocages have a large specific surface area of 349.12 m^2 g^{-1} and contain plenty of micropores and mesopores, which benefit from the carbonization of organic ligands and the catalytic effect of cobalt in the calcination process. As anodes for LIBs, the porous Co–Zn/N–C polyhedral nanocages showed an initial discharge capacity of 809 mA h g^{-1} and a capacity retention of 702 mA h g^{-1} after 400 cycles at a current density of 0.2 A g^{-1}. Furthermore, a reversible capacity of 444 mA h g^{-1} was obtained at a much higher current density of 2 A g^{-1}. The improved electrochemical performance was attributed to the synergistic effect of Zn and Co, the unique porous hollow structure as well as N doping, which relieved the impact of volume changes, maintained perfect electrical conductivity throughout the electrode and enhanced the electrochemical activities of lithium storage.

1. Introduction

Great interest in the development of high-performance and environmentally-friendly energy conversion and storage systems has been significantly growing since it is expected to be one of the promising solutions to solve the global energy crisis and environmental pollution issues.[1–3] As electrochemical energy storage devices, lithium-ion batteries (LIBs) have exhibited a wide range of applications ranging from consumer devices, portable electronics, electric vehicles to large-scale stationary energy storage.[4–6] With more rigorous requirements for hybrid electric vehicles, electric bicycle and flexible/wearable electronics, the development of advanced electrode materials with improved safety, high energy/power density, and easy synthetic and processing approaches has attracted considerable attention.

As is well known, the nature of electrode materials is crucial to the performance of the battery, because the charging–discharging of LIBs is achieved through the intercalation–extraction process of lithium ions in the electrodes. Graphite has been widely used as the anode material in commercial LIBs due to its natural abundance and stable cycling performance; however, it is far from meeting the ever-growing requirements of the next-generation of LIBs due to its low theoretical specific capacity (372 mA h g^{-1}).[7] Thus, seeking alternative anode materials has become an urgent task in building next-generation LIBs with satisfying performance. Recently, a variety of nanostructured Si,[8] Ge,[9] alloy[10] and transition metal oxides[11] featured with high theoretical capacities, have been explored as anode materials due to their special mechanisms for lithium-ion storage. Unfortunately, the poor electronic conductivity and huge volume expansion that persist during the Li insertion and extraction process severely limit their extensive applications in LIBs.

To overcome the aforementioned problems, researchers have continuously focused on engineering carbon-based anode materials with enhanced electrochemical performances in terms of cycling stability and electrical conductivity. Correspondingly, several strategies such as structural design,[12,13] pore building[14,15] and heteroatom doping[16,17]have been extensively investigated to enhance the capacity. Among them, heteroatom doping is the most popular and effective way, whereby the

[a]School of Environmental and Chemical Engineering, Jiangsu University of Science and Technology, Zhenjiang, Jiangsu 212003, PR China. E-mail: jhzhang6@just.edu.cn; aihua.yuan@just.edu.cn

[b]Key Laboratory of the Colloid and Interface Chemistry, Ministry of Education, School of Chemistry and Chemical Engineering, Shandong University, Jinan, 250100, PR China. E-mail: chexsl@sdu.edu.cn

[c]School of the Environment and Safety Engineering, Jiangsu University, Zhenjiang, Jiangsu, 212013, PR China

† Electronic supplementary information (ESI) available. See DOI: 10.1039/c6ta09030c

Published on 14 November 2016. Downloaded by SHANDONG UNIVERSITY on 12/12/2016 07:12:12.

electronic structure of the carbon host can be modified in comparison with that of the undoped counterparts. Recently, various heteroatom-doped carbon materials such as nitrogen,[18] boron,[19] sulfur[20] and phosphorus[21] have been designed and applied as anode materials to enhance Li-storage capability. Nevertheless, they play the respective role in lithium storage depending on their intrinsic properties. The first-principles calculations for the lithium adsorption properties of N- and B-doped materials were reported, which showed that B-doping decreased the Li adsorption energy, while N-doping increased the energy.[22,23] Chen *et al.* investigated the lithium storage performance of highly nitrogen-doped porous carbon from a metal–organic framework (MOF), and the results showed that N-doped porous carbon possessed some exceptional properties, including good electronic conductivity, fast Li^+ diffusion, a low operating voltage, and high theoretical Li storage capacity. Porous carbon, as an alternative, is a type of emerging material with attractive properties for LIBs due to its high conductivity and porosity.[24] Porous structures can not only provide a large electrode–electrolyte contact area and more active sites, but also effectively reduce the distance for Li^+ diffusion. For instance, two-dimensional porous graphitic carbon nanosheets exhibited a very high reversible capacity of 722 mA h g^{-1} as an anode material for LIBs, which was generally ascribed to the high porosity, super high electronic conductivity, and excellent mechanical flexibility and stability.[25] Additionally, the rational construction of anode materials is also of significance to enhance electrochemical performances. Myriad carbon structures with a complex configuration have been explored as LIB anodes. A hollow structure is a kind of well known topology construction and desired competitors by virtue of the characteristic interior space to efficiently relieve the volume expansion. For example, Lou and co-workers reported the synthesis of double-shelled hollow carbon spheres by a facile template method, which manifest improved electrochemical performance.[26]

Inspired by the above-mentioned studies, we described the synthesis of carbon structures with the above-mentioned advantageous features selectively by doping with heteroatoms and metal nanoparticles to improve the electrochemical performance. MOFs have been demonstrated as ideal metals, carbon and other element sources, and self-sacrificial templates for the preparation of porous carbon matrix composites.[24,27–31] Direct pyrolysis of MOFs was recently found to be a facile and versatile route to synthesize microporous carbon with a narrow pore-size distribution and extremely high surface area.[25] In this work, bimetallic Co/Zn embedded N-doped carbon (Co–Zn/N–C) polyhedral nanocages were devised and synthesized by pyrolysis of a core–shell Co(2-methyl-imidazole)$_2$ (ZIF-67) @Zn(2-methyl-imidazole)$_2$ (ZIF-8) (ZIF-67@ZIF-8) precursor under an Ar atmosphere. To the best of our knowledge, MOF-derived N-doped porous carbon materials embedded with a bi-metal had rarely been reported for the investigation of LIBs.[29] During the pyrolysis process, organic ligands bridging metal cores were transformed to a porous carbon network by nitrogen doping; simultaneously, metal cations were *in situ* reduced to metallic Zn and Co which were retained in the carbon matrix. The as-prepared carbon-involved structures perfectly inherited the morphological characteristics of the parent ZIF-8@ZIF67 precursors. Such a unique structure endues the composites with excellent electrochemical performance as anode materials for LIBs.

2. Experimental section

Chemicals

Zinc nitrate hexahydrate ($Zn(NO_3)_2 \cdot 6H_2O$, ≥99.0%), cobalt chloride ($CoCl_2 \cdot 6H_2O$, ≥98.0%) and 2-methylimidazole (2-MeIm, ≥99.0%), and polyvinylpyrrolidone (PVP, average MW: 10 000) were purchased from Aladdin Chemical Co. Methanol was obtained from the traditional Chinese medicine Reagent Co. All the chemicals were used without further purification.

Preparation of ZIF-8 crystals

In a typical synthesis of ZIF-8, zinc nitrate hexahydrate (300 mg) and PVP (1200 mg) were dissolved in methanol (60 mL); another stock solution was prepared by dissolving 2-MeIM (830 mg) in methanol (60 mL). The two solutions were mixed under intense stirring for 30 min. Then the final mixture was stewed at room temperature for 24 h. ZIF-8 nanocrystals were obtained from the milky dispersion by centrifugation at 8000 rpm for 3 min and washed with ethanol three times, and dried at 60 °C in a vacuum oven.

Preparation of ZIF-67 crystals

The synthesis procedures were similar to the preparation of ZIF-8 crystals, except that the first solution was obtained by dissolving cobalt chloride (177 mg) and PVP (600 mg) in methanol (60 mL).

Preparation of core–shell ZIF-8@ZIF-67 crystals

Briefly, ZIF-8 seeds (80 mg) were firstly well-dispersed in methanol (10 mL) under sonication for 30 min. After stirring for 20 min, a methanolic solution of cobalt chloride (177 mg, 6 mL) and another methanolic solution of MeIm (895 mg, 6 mL) were immediately injected. After stirring for another 5 min, the mixture was transferred into an autoclave and kept at 100 °C for 12 h. After cooling to room temperature, the resulting sample was collected by centrifugation, washed several times with ethanol, and dried at 60 °C in a vacuum box.

Preparation of porous Co–Zn/N–C polyhedral nanocages

Core-shell ZIF-8@ZIF-67 crystals were calcined under an Ar atmosphere at 800 °C for 3 h at a heating rate of 2 °C min^{-1}. As control experiments, ZIF-8 derived N-doped C and ZIF-67 derived Co/N–C were prepared by pyrolysis of their respective precursors under the same calcination conditions, respectively.

Structural characterization

Transmission electron microscopy (TEM, JEM-1011 and JEOL-2100) and field-emission scanning electron microscopy (FESEM, JSM-7600F) were used to observe the morphology and

 This journal is © The Royal Society of Chemistry 2016

Published on 14 November 2016. Downloaded by SHANDONG UNIVERSITY on 12/12/2016 07:12:12.

microstructure. Elemental analysis is carried out with a Vario EL III Elemental Analyzer. The powder X-ray diffraction (XRD) patterns were measured using a Bruker D8 Advance X-ray diffractometer using Cu Kα radiation (λ = 1.5418 Å). Thermogravimetric analysis (TGA) was carried out using a Mettler Toledo TGA/SDTA851 thermal analyzer under a nitrogen atmosphere at a heating rate of 10 °C min^{-1}. The Raman spectra were obtained at ambient temperature using a Leica DM2700 microscope with a YAG laser (50 mW at 532 nm) and a diffraction grating of 1800 L mm^{-1}. The Brunauer–Emmett–Teller (BET) surface area and pore size distributions were performed with a Micromeritics ASAP2020 instrument by N_2 adsorption–desorption isotherms at 77 K. X-ray photoelectron spectroscopy (XPS, Perkin-Elmer model PHI 5600) using Al Kα as the X-ray source was applied to analyze the chemical state of the surface of the samples.

Electrode fabrication and electrochemical measurements

The electrochemical behavior of porous Co–Zn/N–C polyhedral nanocages was examined using CR2032 coin-type cells with lithium serving as the counter electrode. The working electrode was prepared by mixing 75% of the active materials, 9% of the polymer binder (PVDF), 8% of CNTs (carbon nanotubes) and 8% of the conductive material (acetylene black) and the obtained mixture was dispersed in *N*-methyl pyrrolidone (NMP) solution. Then, the slurry was subsequently brushed on copper foil and dried at 100 °C for 24 h in a vacuum box. The nonaqueous electrolyte used in the cells was 1.00 mol L^{-1} $LiPF_6$ dissolved in ethylene carbonate and diethyl carbonate (EC : DEC, 1 : 1 in vol%). A Celgard 2400 microporous polypropylene membrane and Li foil were used as the separator and counter electrode, respectively. The cells were assembled in an argon-filled glovebox with the moisture and oxygen content less than 1 ppm. The electrode capacity was measured using the galvanostatic cycling of the cells on a LAND CT-2001A in the voltage range of 0.01–3 V *versus* Li^+/Li at room temperature (25 °C). The cyclic voltammetry (CV) curves were recorded using a CHI-760E workstation (Shanghai, China) between 0.01 and 3 V at a scan rate of 0.1 mV s^{-1}. The electrochemical impedance spectra (EIS) of the cells were also recorded using the same instrument by applying a sine wave with the amplitude of 5 mV over the frequency range from 100 kHz to 0.01 Hz.

3. Results and discussion

The schematic diagram of the synthetic route for porous Co–Zn/N–C polyhedral nanocages is shown in Fig. 1. The core–shell ZIF-8@ZIF-67 precursor was assembled by a seed-mediated growth technique. ZIF-8 and ZIF-67 were selected as candidates for the preparation of precursor core–shell structures, which was attributed to the same topological structure of ZIF-67 as that of ZIF-8 combined with metal cations four-coordinated with 2-methylimidazole.[32,33] As clearly seen in the powder XRD of Fig. S1 (ESI†), the diffraction patterns of the as-prepared ZIF-8, ZIF-67, and ZIF-8@ZIF-67 are similar relying on the similar lattice constants and crystal structures of ZIF-8 (core) and ZIF-67 (shell), well ensuring that the ZIF-67 shell can homogeneously grow on the surface of ZIF-8 crystals. The strong and sharp profiles further confirm the high crystallinity of the three samples. To further confirm the structural information of core–shell structured ZIF-8@ZIF-67, EDX line analysis and chemical mappings of our synthesized samples were provided. Across the radial direction (yellow-line) of a polyhedral nanocage (see the scanning TEM (STEM) image in Fig. S4A, ESI†), $L_{\alpha 1}$ elemental line profiles clearly indicate that the cobalt element has maximum values in the shell; while the zinc element has maximum values in the core in this polyhedral nanocage. Therefore, the line profiles of Zn and Co components along the investigated line distinctly reveal the core–shell nature of the as-fabricated ZIF-8@ZIF-67. In addition, chemical mapping images of the two elements Zn and Co in the polyhedral nanocage also show the identical structural information (Fig. S4B, ESI†). The thermal stabilities of the as-prepared ZIF-8 and ZIF-67@ZIF-8 were investigated by TGA under a N_2 atmosphere. As shown in Fig. S2 (ESI†), ZIF-8 undergoes a clear weight-loss step from 560 °C to 800 °C, which is ascribed to the decomposition of ZIF-8. The decomposition curve of ZIF-67@ZIF-8 presents the first weight loss in the temperature range of 470–560 °C, corresponding to the decomposition of ZIF-67. The second weight loss from 560 to 800 °C could be attributed to the

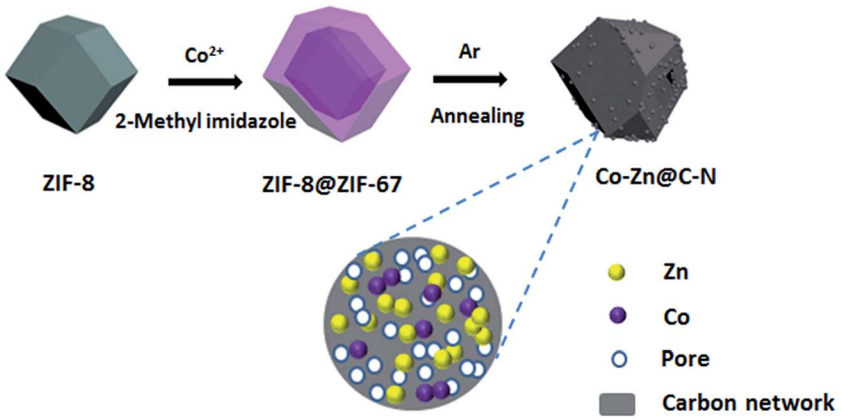

Fig. 1 Schematic illustration of the synthesis route to porous Co–Zn/N–C polyhedral nanocages.

Published on 14 November 2016. Downloaded by SHANDONG UNIVERSITY on 12/12/2016 07:12:12.

decomposition of ZIF-8. Thus the calcination temperature of 800 °C is fixed to confirm the complete decomposition of ZIF-67@ZIF-8.[34]

The morphologies and structures of ZIF-8, ZIF-8@ZIF-67 and their derivatives yielded by calcinations at 800 °C were thoroughly investigated by FESEM and TEM. Fig. S3A and B (ESI†) show FESEM images of ZIF-8 and ZIF-67 crystals before carbonization, revealing that these crystals exhibit a regular rhombic dodecahedral morphology composed of well-defined rhombus faces and straight edges. The average size of ZIF-8 is about 250 nm, smaller than that of ZIF-67 polyhedra. Due to the similar structures and unit cell parameters between ZIF-8 and ZIF-67, the ZIF-8@ZIF-67 core–shell structures were successfully synthesized *via* the seed-mediated route. Fig. S3C (ESI†) indicates that the morphology of ZIF-8@ZIF-67 with a smooth surface is similar to that of ZIF-8, and the average size of the polyhedra is about 600 nm. The inset is a typical TEM image of a single ZIF-8@ZIF-67 crystal, consistent with the results of FESEM. After the pyrolysis treatment of ZIF-8 under an Ar atmosphere at 800 °C for 3 h, the carbonized products substantially retain the original morphology of the original ZIF-8 crystals. Nevertheless, the surface became rough and concave; the structure showed remarkable shrinkage (Fig. S3D†). This could be associated with the massive loss of organic components during the annealing process. As revealed in Fig. 2A, the ZIF-8@ZIF-67 derived products well-retained the polyhedral shape from the parental template. Meanwhile Co–Zn/N–C polyhedral nanocages were intimately and densely decorated with a large number of Co nanoparticles embedded in the carbon matrix due to the magnetic attraction during heating treatment. Fig. 2B displays that Co–Zn/N–C polyhedra are porous nanocages with a uniform size of around 500 nm. It can be explained that ZIF-8@ZIF-67 precursors decomposed to produce gas, which forced metal ions to move outside, leading to the formation of hollow structures with porous shells.[35] Fig. 2C displays the high-magnification TEM image of porous Co–Zn/N–C polyhedral nanocages, which shows that the wall of the nanocages is about 55 nm in thickness. To ensure the phase structure of decomposed products, the porous polyhedral nanocages were investigated by XRD. After calcining, the characteristic peaks of ZIF-8 and ZIF-67 disappeared completely, and the three apparent diffraction peaks located at $2\theta = 44.2°$, 51.6°, and 75.9° can be indexed to the (111), (200) and (220) planes of fcc-structured metallic Co (PDF no. 89-4307), demonstrating the formation of Co nanoparticles after calcination of the ZIF-8@ZIF-67 precursor. In addition, a weak and broad peak at approximately 26° was attributed to the (002) peak of graphitic carbon. No diffraction peaks corresponding to zinc or zinc compounds are observed in the pattern; but XPS detection and elemental mapping confirm the presence of metallic Zn and will be discussed below. Raman spectrum was analyzed to further characterize the as-prepared samples. As shown in Fig. S5 (ESI†), the two broad peaks at 1357 and 1558 cm^{-1} are ascribed to the D and G bands of carbon, respectively. More specifically, the two peaks can be attributed to E_{2g} mode of graphite related to the vibration of sp^2-bonded carbon atoms in a 2D hexagonal lattice (such as in a graphene layer) and an A_{1g} mode of graphite related to the disorder due to the finite particle size effect or lattice distortion of the graphite crystals. The intensity ratio of the D-G band, I_D/I_G, can give reliable information on the degree of graphitization.[36] It is found that the composites have a higher I_G/I_D, implying the excellent graphitization degree of the porous carbon, and these results are consistent with the XRD pattern.

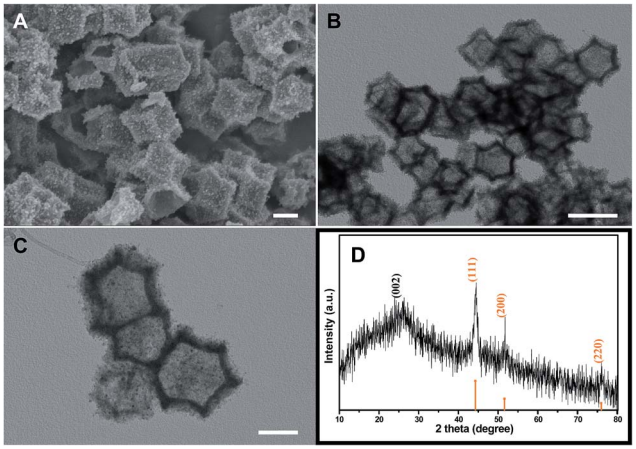

Fig. 2 ZIF-8@ZIF-67 derived porous Co–Zn/N–C polyhedral nanocages: (A) SEM image; (B) low-magnification TEM image; (C) high-magnification TEM image; (D) XRD pattern. Scale bars: (A) 200 nm (B) 500 nm and (C) 200 nm.

More structural information was further revealed by high-magnification TEM, HRTEM and EDX characterization. As shown in Fig. S6A (ESI†), the nanoparticles were homogeneously embedded in a polyhedral nanocage matrix, with an average size of about 8 nm. No significant aggregates were observed. Interestingly, a number of flexible carbon nanotubes (CNTs) with a diameter of ~10 nm that extended from the surface of the carbon framework could be clearly observed (Fig. S6B†). In the previous report, it is shown that with the presence of inert gases, Co nanoparticles can catalyze the production of CNTs from ethene.[37] Moreover, it is widely accepted that CNTs are generated *in situ* under the catalytic effect of cobalt nanoparticles at high temperature and a sufficient partial pressure of Ar.[30] The high-magnification TEM in Fig. 3A reveals that cobalt nanoparticles are encapsulated in a carbon nanoshell and the HRTEM image in Fig. 3B exhibits a single completely wrapped metallic cobalt nanoparticle with the (111) lattice fringes (a spacing of 0.206 nm). No lattice fringes ascribed to CoO or Co_3O_4 have been found, which is in accordance with the results of XRD. Another group of fringes with a distance of 0.34 nm can also be clearly seen in Fig. 3B, indicating a highly graphitized carbon shell. The continuous graphitic carbon layers, tightly wrapping around the cobalt nanoparticles, can prevent Co nanoparticles from aggregation and oxidation. Additionally, Fig. 3C shows the energy dispersive spectrum (EDS) and the inset is its corresponding STEM image. The results reveal the existence of C, N, Co, Zn and Cu elements, wherein the Cu signal is ascribed to the copper grid. The elemental mapping images in Fig. 3D point out a highly

 This journal is © The Royal Society of Chemistry 2016

Published on 14 November 2016. Downloaded by SHANDONG UNIVERSITY on 12/12/2016 07:12:12.

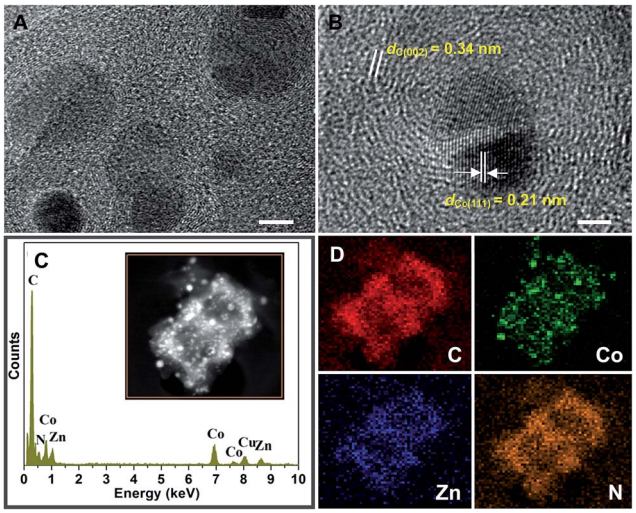

Fig. 3 (A) A high-magnification TEM image of porous Co–Zn/N–C polyhedral nanocages; (B) HRTEM image of a single completely wrapped metallic cobalt nanoparticle; (C and D) EDS and elemental mappings of porous Co–Zn/N–C polyhedral nanocages indicating the distribution of the C, Co, Zn, and N elemental mappings, revealing the homogeneous dispersion throughout the polyhedral nanocages, and the inset is the corresponding STEM image. Scale bars: (A) 5 nm and (B) 2 nm.

uniform distribution of Co, Zn, C and N, confirming the formation of a bimetal embedded in the porous N-doped carbon matrix. The embedding and doping of Co and Zn enhanced the conductivity of the samples substantially and promoted graphitization of carbon in the as-synthesized composites simultaneously.

XPS was obtained to further investigate the surface characteristics of porous Co–Zn/N–C polyhedral nanocages and the corresponding full spectrum is indicated in Fig. S7 (ESI†). Peaks corresponding to Co, Zn, N and C are clearly observed, which suggest that there are Co (1.73%), Zn (2.09%), N (12.76%), and C (83.42%) elements on the surface of the porous Co–Zn/N–C polyhedral nanocages. The high resolution C 1s spectrum in Fig. 4A can be fitted to the three peaks of C–C (284.6 eV, sp^2-hybridized carbon), C–O (286.2 eV), and C=O/C=N (287.7 eV), which indicated an asymmetric tail at a higher binding energy and this is an ordinary feature for N-doped carbon materials. N actually comes from the decomposed 2-methylimidazole ligands and also provides evidence for the successful doping. The high resolution N 1s spectrum (Fig. 4B) can be deconvoluted to the three sub-peaks of pyridinic-N (398.7 eV), pyrrolic-N (399.8 eV), and graphitic-N (401.0 eV).[38] As shown in Fig. 4C, two notable peaks at 780.8 and 795.9 eV are present in the Co 2p spectrum, which can be assigned to Co(0).[38] Similarly, the Zn 2p

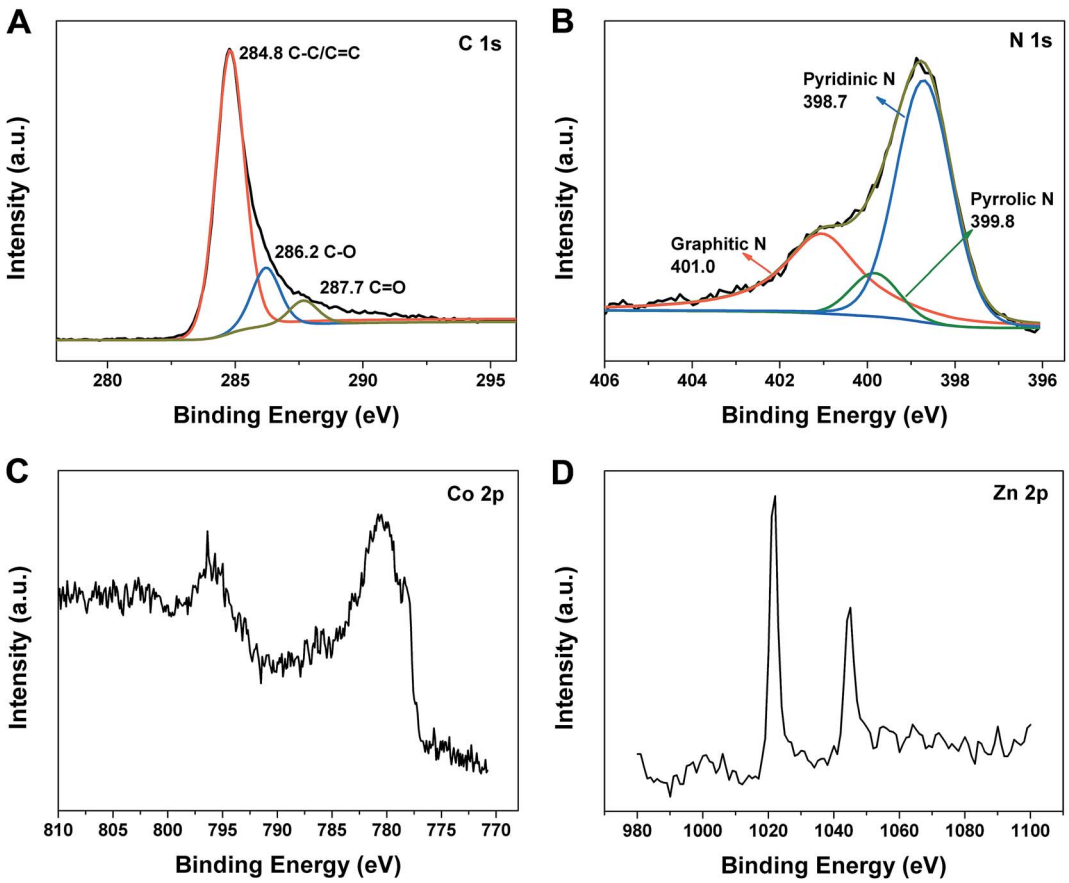

Fig. 4 XPS spectra of the porous Co–Zn@N–C polyhedral nanocages: (A) survey scan spectrum; (B) high-resolution N 1s spectrum; (C) high-resolution Co 2p spectrum; (D) high-resolution Zn 2p spectrum.

Published on 14 November 2016. Downloaded by SHANDONG UNIVERSITY on 12/12/2016 07:12:12.

spectrum (Fig. 4D), shows two evident peaks at about 1021.2 and 1044.2 eV, which can be assigned to metallic Zn.[39] Because of the low boiling point of zinc (908 °C), it will evaporate during calcination of ZIF-8 at 800 °C.[24] However, metallic Zn was retained in the product after calcining ZIF-8@ZIF-67, possibly because the outer shell of ZIF-67 played the role of blocking the partial release of Zn. The residual Zinc metal is small in quantity or size, which cannot be detected by XRD.

The surface profile is the key factor for the electroactive materials in electrical storage applications and can be investigated by nitrogen adsorption–desorption isotherms at 77 K shown in Fig. 5A. For porous Co–Zn/N–C polyhedral nanocages, the rapid rise of the adsorption at a low pressure range ($P/P_0 \sim 0$) reveals the presence of a large amount of micropores. The hysteresis loop appears at the P/P_0 of 0.4–0.98, caused by the presence of mesopores. Hence, there are two types of pores in the as-prepared polyhedral nanocages. From the pore-size distribution curve based on the BJH method in the inset of Fig. 5B, one type is mesopores with a narrow pore-size distribution between 2.0 and 4.5 nm, and another type is micropores with a size of 0.68 nm. Porous Co–Zn/N–C polyhedral nanocages exhibit a high specific surface area of 349.12 $m^2\ g^{-1}$ and a total pore volume of 0.304 $cm^3\ g^{-1}$. The larger surface area and pore volume can offer more active sites for the electrochemical reactions and ensure an efficient transport pathway between the electrolyte and the active electrode materials.

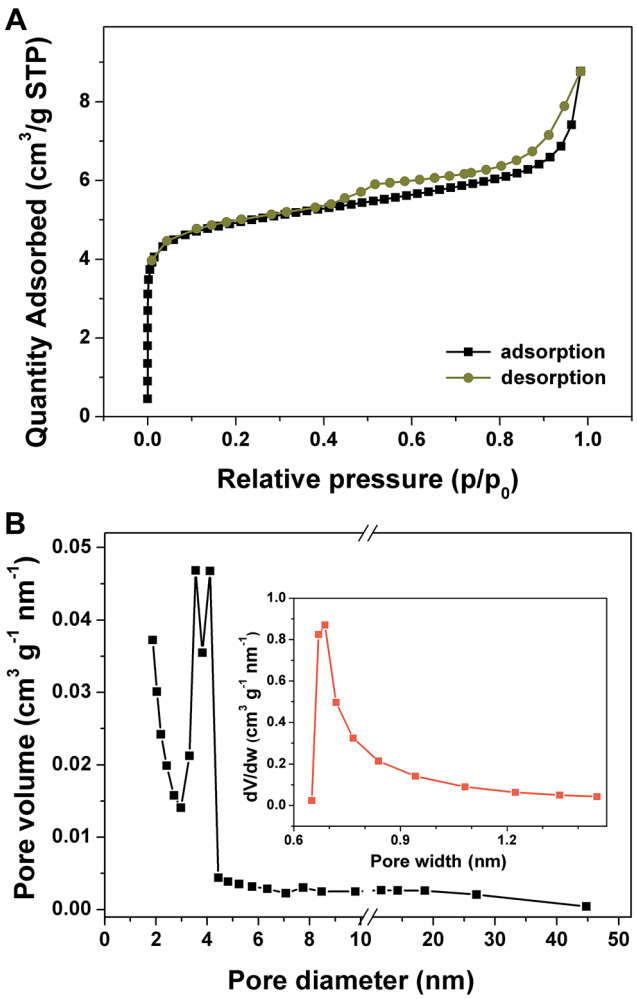

Fig. 5 (A) Nitrogen adsorption–desorption isotherms and (B) pore-size distribution curves of porous Co–Zn/N–C polyhedral nanocages.

Considering that porous Co–Zn/N–C polyhedral nanocages show some advantageous features for LIB application, involving an anisotropic hollow structure, larger specific surface area and pore volume, the electrochemical lithium-storage properties were investigated by the standard half-cell configuration. The electrochemical properties of the as-obtained product is first investigated by CV. Fig. 6A indicates the first three consecutive CV curves of the electrode of Co–Zn/N–C polyhedral nanocages between 0.01 and 3.0 V at a scan speed of 0.1 mV s^{-1} at room temperature. Notably, the first cycle displays a different CV curve from the following cycles, especially for the discharge band. For the first discharge process, a strong peak is observed at 0.5 V, which is usually attributed to the occurrence of side reactions on the electrode surfaces and interfaces due to the solid-electrolyte interphase (SEI) film.[40] The peak vanishes during the subsequent cycles; it is inferred that some irreversible reactions have occurred, the formation of a SEI film. A distinct peak that appears at 0.2 V during the discharge in the second and third cycles is ascribed to the generation of a new SEI film during the charge and discharge processes.[24] The cathodic peak at ~1.4 V confirmed the synergetic effect of Co and Zn NPs and the N-doped analogous graphene framework in the Co–Zn/N–C composite toward the enhanced electrochemical performance.[41] The cathodic peaks at ~0.9 V in the first sweep can be ascribed to the lithium insertion into the electrode as Li_xZn.[42] During the anodic cycles, the peak can be observed at about 0.25 V, which is attributed to the reversible extraction of lithium from the Li_xZn alloy to the formation of metallic Zn and Li in several steps.[41–43] In addition, one broad oxidation peak is observed between 1.0 and 1.5 V. which corresponds to the delithiation of defective sites within the carbon matrix.[44] It is noted that CV curves almost overlap, indicating the stable and good reversibility. Fig. 6B shows the representative discharge–charge voltage profiles within a cutoff voltage window of 0.01–3.0 V at 0.2 A g^{-1}. The initial discharge and charge capacities are found to be 863.3 and 509.6 mA h g^{-1}, respectively. The low coulombic efficiency (CE) of 59% may be caused by the irreversible capacity loss, including the inevitable formation of the SEI and decomposition of the electrolyte, which is common for most anode materials. The porous Co–Zn/N–C polyhedral nanocages exhibit sloping voltage (*vs.* capacity) profiles, similar to those of porous carbon materials for application in LIBs.[45,46] Remarkably, the long plateaus at about 0.84 V shown in the first discharge disappears during the second and third discharge, suggesting that the reductive decomposition of the electrolyte is effectively prevented due to the formation of the SEI film in the first discharge, which can greatly relieve the irreversible capacity loss of the following cycles. Therefore, the CE increases rapidly to 95% in the second cycle and the corresponding discharge and charge capacities of the 2nd cycle are 531.3 and 504.9 mA h g^{-1}, respectively. After the 10th cycle, the discharge capacity of porous Co–Zn/N–C polyhedral nanocages

 This journal is © The Royal Society of Chemistry 2016

Published on 14 November 2016. Downloaded by SHANDONG UNIVERSITY on 12/12/2016 07:12:12.

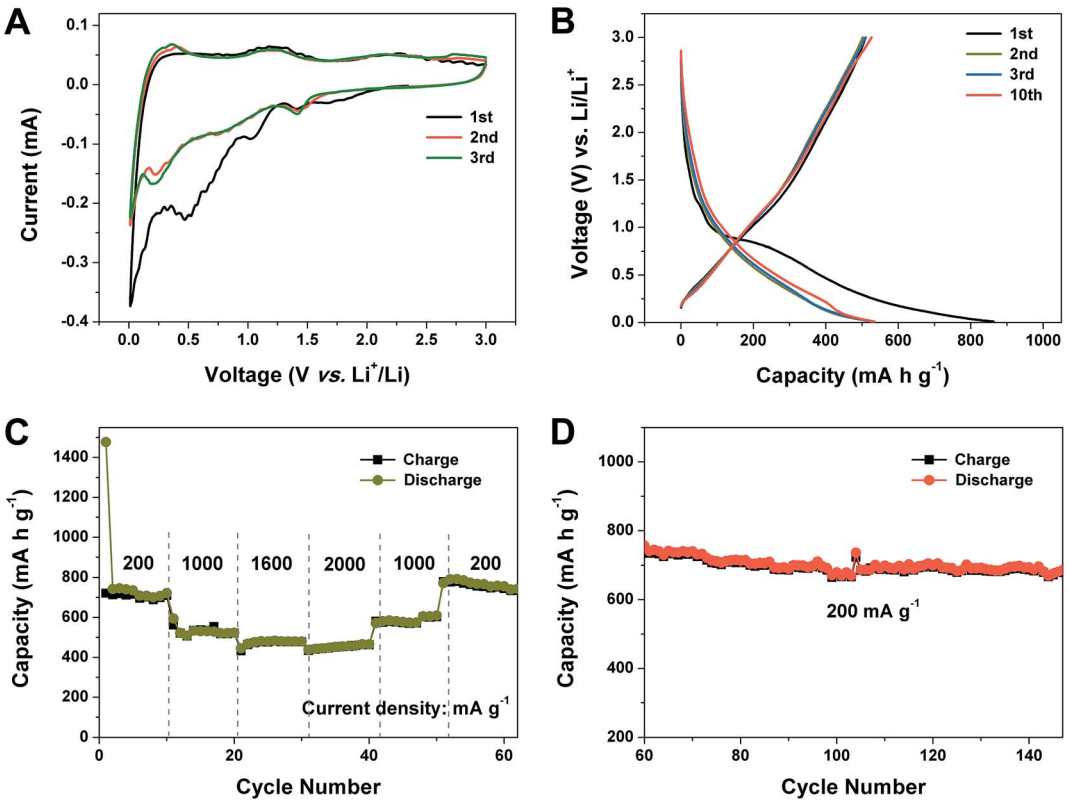

Fig. 6 Electrochemical performances of porous Co–Zn/N–C polyhedral nanocages as anode materials for LIBs: (A) the first three consecutive CVs in the voltage range of 0.01–3.0 V *vs.* Li/Li^+ at a scan rate of 0.1 mV s^{-1}; (B) discharge–charge curves at a current density of 0.2 A g^{-1}; (C) rate performance at different current densities between 0.01 and 3.0 V; (D) continued cycling performance of the porous Co–Zn/N–C polyhedral nanocage electrode (the same cell as for (C)) over 80 cycles at 0.2 A g^{-1}.

is still maintained at 537.8 mA h g^{-1}, and the CE steadily reached around 98.4%. The results are also in good agreement with that of the CV curves.

The rate capability of porous Co–Zn/N–C polyhedral nanocages was evaluated at various current densities from 0.2 to 2 A g^{-1} as presented in Fig. 6C. As can be seen, the reversible capacities remain stable and decrease regularly with an increased rate. The high-rate capacities of 708, 530, 480 and 444 mA h g^{-1} can be obtained at rates of 0.2, 1, 1.6, and 2 A g^{-1}, respectively, showing remarkable rate capability. Moreover, the discharge capacity can still be recovered to 683 mA h g^{-1} when the current density went back to 0.2 A g^{-1} after more than 145 cycles (Fig. 6D), indicating that porous Co–Zn/N–C polyhedral nanocages have great potential as a high-rate anode material in LIBs.

The cycling performance together with the CE of porous Co–Zn/N–C polyhedral nanocages is demonstrated at a constant current density of 0.2 A g^{-1} between 0.01 and 3 V in Fig. 7.

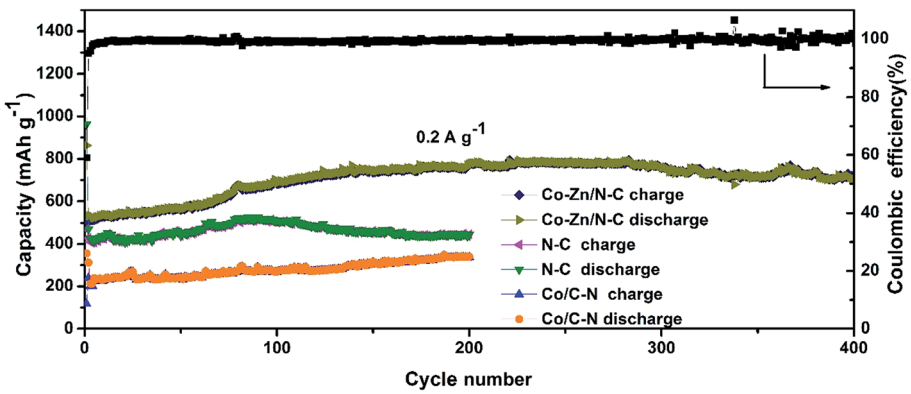

Fig. 7 Cycling performance of porous Co–Zn/N–C polyhedral nanocages, N-doped C, and Co/N–C at a current of 0.2 A g^{-1}.

Published on 14 November 2016. Downloaded by SHANDONG UNIVERSITY on 12/12/2016 07:12:12.

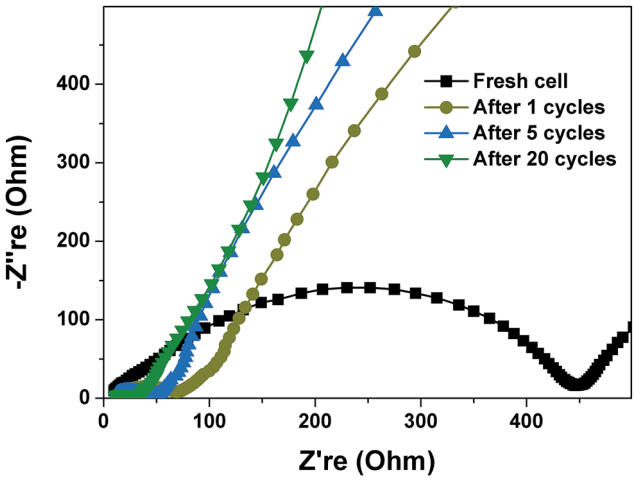

Fig. 8 Electrochemical impedance spectra (EIS) of porous Co–Zn/N–C polyhedral nanocages at a fresh cell and after the 1st, 5th and 20th cycles at 0.2 A g^{-1}.

Remarkably, after a few discharge–charge cycles, porous Co–Zn/N–C polyhedral nanocages exhibit excellent cyclic capacity retention and the CE steadily remains ~100%. Although the initial capacity is low for the first cycle, the capacity of porous Co–Zn/N–C polyhedral nanocages rises gradually during the initial 200 cycles, which could be attributed to the gradual penetration of the electrolyte all over the porous active material during cycling at a low current density and the progressive generation of electrochemically active polymeric films. Till the 400th charge–discharge cycle, a reversible capacity of 702 mA h g^{-1} can still be retained, almost 2 times the theoretical capacity of commercial graphite (372 mA h g^{-1}). For comparison, ZIF-8 derived N-doped C and ZIF-67 derived Co/N–C were also obtained by the same calcination approach, and the capacity profile for 200 charge–discharge cycles is shown in Fig. 7. The reversible capacities of N-doped C and Co/N–C can be retained at ~444 and 340 mA h g^{-1} at the end of 200 charge–discharge cycles, which also present decent cyclic stability. Nevertheless, the reversible capacities of N-doped C and Co/N–C are lower than those of porous Co–Zn/N–C polyhedral nanocages. After cycling, the initial structure of Co–Zn/N–C polyhedral nanocages can be well preserved after 30 discharge–charge cycles at 200 mA g^{-1} (Fig. S8, ESI†). The lithium-storage ability of porous Co–Zn/N–C polyhedral nanocages in the current study is superior to that of many other porous carbon-based anodes for LIBs as indicated in Table S1 (ESI†). The above results clearly demonstrate that the Co–Zn bimetal is beneficial for the capacity improvement, possibly explained by the synergistic effect between Co and Zn. Firstly, Co particles can improve electronic conductivity and increase the structural integrity, and Zn particles play an important role in increasing the active material utilization of Co–Zn/N–C polyhedral nanocages.[47] Secondly, the essential properties of zinc, such as the lithium alloying reaction, could also contribute to the electrochemical performance. Last but not the least, the porous structure and N-doping also play an important role in relieving the impact of volume changes during the repeated discharge/charge process, maintaining perfect electrical conductivity and integrity of the structure and enhancing electrochemical activities for lithium storage. The N atoms especially for pyridinic and pyrrolic N can provide more active sites for Li ions and thus accelerate the transportation of electrons and Li ions in the electrode. As a result, the prepared product shows a higher reversible capacity as an anode material for LIBs than graphite.[24]

To further understand lithium-storage properties, an AC impedance measurement was employed. Electrochemical impedance spectra (EIS) of porous Co–Zn/N–C polyhedral nanocages were investigated at a fresh cell and after the 1st, 5th and 20th cycles at 0.2 A g^{-1}, as shown in Fig. 8. The four Nyquist plots consist of one semicircle in the high-frequency region and a straight line in the low-frequency region. The semicircle portion is related to the reactions occurring on the electrode–electrolyte interface, which reflects the charge transfer impedance and SEI impedance. The larger the diameter of the semicircle, the larger the charge transfer resistance. It can be seen that porous Co–Zn/N–C polyhedral nanocages cycled exhibit a lower charge transfer resistance than fresh cells, which indicates that the fresh cell has the highest charge transfer resistance. This result suggests that the higher diffusivity of lithium ions with increasing charge–discharge cycles can reduce the charge transfer resistance.

4. Conclusions

In summary, this work provides a facile and controllable route to synthesize porous Co–Zn/N–C polyhedral nanocages on a large scale *via* solid-state thermolysis of ZIF-67@ZIF-8 as the Co, Zn, N, and C source and sacrificial template. The well-defined porous Co–Zn/N–C polyhedral nanocages were obtained with the uniform dispersion of Co along with Zn nanoparticles and N-doping in the carbon framework. When evaluated as an anode material for LIBs, porous Co–Zn/N–C polyhedral nanocages exhibit enhanced reversible capacity, excellent cyclic stability (702 mA h g^{-1} after 400 cycles) and good rate capability up to 2 A g^{-1}. The improved electrochemical performance of porous Co–Zn/N–C polyhedral nanocages could be ascribed to the unique structural features, which not only facilitate the electrolyte diffusion and intercalation of Li-ions into the active phases, but also better the volume change of anodes during the repeated Li-ion insertion/extraction. Therefore, the porous Co–Zn/N–C polyhedral nanocages could be one of the promising anode materials for high-performance LIBs. Most importantly, the facile solid-phase conversion approach can be easily extended to the scaled-up synthesis of other porous carbon-based functional materials with well-defined morphologies and architectures.

Acknowledgements

The work was financially supported by the Natural Science Foundation of China (No. 21371108, 51672114, 51603091), the Fundamental Research Funds of Shandong University (No. 2016JC033), the Natural Science Foundation of Jiangsu Province (No. BK20141393), the Opening Project of the State Key Laboratory of Fire Science (No. HZ2015-KF03), and Jiangsu Qinglan Project.

 This journal is © The Royal Society of Chemistry 2016

Published on 14 November 2016. Downloaded by SHANDONG UNIVERSITY on 12/12/2016 07:12:12.

References

1 H. Jesse Smith, *Science*, 2016, **351**, 236.
2 N. Recham, J. N. Chotard, L. Dupont, C. Delacourt, W. Walker, M. Armand and J. M. Tarascon, *Nat. Mater.*, 2010, **9**, 68.
3 S. Gao, Y. Lin, X. C. Jiao, Y. F. Sun, Q. Q. Luo, W. H. Zhang, D. Q. Li, J. L. Yang and Y. Xie, *Nature*, 2016, **529**, 68.
4 X. L. Dong, L. Chen, J. Y. Liu, S. Haller, Y. G. Wang and Y. Y. Xia, *Sci. Adv.*, 2016, **2**, e1501038.
5 Y. T. Li, W. D. Zhou, S. Xin, S. Li, J. L. Zhu, X. J. Lv, Z. M. Cui, Q. X. Jia, J. S. Zhou, Y. S. Zhao and J. B. Goodenough, *Angew. Chem., Int. Ed.*, 2016, **55**, 9965.
6 J. H. Lee, C. S. Yoon, J. Y. Hwang, S. J. Kim, F. Maglia, P. Lamp, S. T. Myung and Y. K. Sun, *Energy Environ. Sci.*, 2016, **9**, 2152.
7 L. Zhang, H. B. Wu, S. Madhavi, H. H. Hng and X. W. Lou, *J. Am. Chem. Soc.*, 2012, **134**, 17388.
8 N. Lin, Y. Han, J. Zhou, K. L. Zhang, T. J. Xu, Y. C. Zhu and Y. T. Qian, *Energy Environ. Sci.*, 2015, **8**, 3187.
9 W. H. Li, Z. Z. Yang, J. X. Cheng, X. W. Zhong, L. Gu and Y. Yu, *Nanoscale*, 2014, **6**, 4532.
10 J. W. Jung, W. H. Ryu, J. Shin, K. Park and I. D. Kim, *ACS Nano*, 2015, **9**, 6717.
11 L. C. Yang, X. Li, Y. P. Ouyang, Q. S. Gao, L. Z. Ouyang, R. Z. Hu, J. Liu and M. Zhu, *ACS Appl. Mater. Interfaces*, 2016, **8**, 19987.
12 P. Remith and N. Kalaiselvi, *Phys. Chem. Chem. Phys.*, 2016, **18**, 15854.
13 J. Liu, N. P. Wickramaratne, S. Z. Qiao and M. Jaroniec, *Nat. Mater.*, 2015, **14**, 763.
14 C. Y. Zhu and T. Akiyama, *Green Chem.*, 2016, **18**, 2106.
15 F. C. Zheng, G. L. Xia, Y. Yang and Q. W. Chen, *Nanoscale*, 2015, **7**, 9637.
16 T. Q. Lin, I. W. Chen, F. X. Liu, C. Y. Yang, H. Bi, F. F. Xu and F. Q. Huang, *Science*, 2015, **350**, 1508.
17 Z. Q. Zhu, S. W. Wang, J. Du, Q. Jin, T. R. Zhang, F. Y. Cheng and J. Chen, *Nano Lett.*, 2014, **14**, 153.
18 Q. F. Wang, R. Q. Zou, W. Xia, J. Ma, B. Qiu, A. Mahmood, R. Zhao, Y. C. Yang, D. G. Xia and Q. Xu, *Small*, 2015, **11**, 2511.
19 Y. Q. Yang, J. N. Zhang, X. C. Wu, Y. S. Fu, H. X. Wu and S. W. Guo, *J. Mater. Chem. A*, 2014, **2**, 9111.
20 Y. Yan, Y. X. Yin, S. Xin, Y. G. Guo and L. J. Wan, *Chem. Commun.*, 2012, **48**, 10663.
21 C. Z. Zhang, N. Mahmood, H. Yin, F. Liu and Y. L. Hou, *Adv. Mater.*, 2013, **25**, 4932.
22 D. H. Wu, Y. F. Li and Z. Zhou, *Theor. Chem. Acc.*, 2011, **130**, 209.
23 Z. Zhou, X. Gao, J. Yan, D. Song and M. Morinaga, *Carbon*, 2004, **42**, 2677.
24 F. C. Zheng, Y. Yang and Q. W. Chen, *Nat. Commun.*, 2014, **5**, 5261.
25 L. Chen, Z. Y. Wang, C. N. He, N. Q. Zhao, C. S. Shi, E. Z. Liu and J. J. Li, *ACS Appl. Mater. Interfaces*, 2013, **5**, 9537.
26 C. F. Zhang, H. B. Wu, C. Z. Yuan, Z. P. Guo and X. W. Lou, *Angew. Chem., Int. Ed.*, 2012, **51**, 9592.
27 J. T. Zhang, H. Hu, Z. Li and X. W. Lou, *Angew. Chem., Int. Ed.*, 2016, **55**, 3982.
28 D. Ji, H. Zhou, J. Zhang, Y. Y. Dan, H. X. Yang and A. H. Yuan, *J. Mater. Chem. A*, 2016, **4**, 8283.
29 B. Y. Guan, L. Yu and X. W. Lou, *Energy Environ. Sci.*, 2016, **9**, 3092.
30 B. Y. Xia, Y. Yan, N. Li, H. B. Wu, X. W. Lou and X. Wang, *Nat. Energy*, 2016, **1**, 15006.
31 Z. Q. Li and L. W. Yin, *ACS Appl. Mater. Interfaces*, 2015, **7**, 4029.
32 K. S. Park, Z. Ni, A. P. Cote, J. Y. Choi, R. Huang, F. J. Uribe-Romo, H. K. Chae, M. O'Keeffe and O. M. Yaghi, *PNAS*, 2006, **103**, 10186.
33 A. P. Rahul Banerjee and B. Wang, *Science*, 2008, **319**, 939.
34 F. Zheng, Y. Yang and Q. Chen, *Nat. Commun.*, 2014, **5**, 5261.
35 L. Hu, Y. M. Huang, F. P. Zhang and Q. W. Chen, *Nanoscale*, 2013, **5**, 4186.
36 J. H. Zhang, Q. H. Kong, L. W. Yang and D. Y. Wang, *Green Chem.*, 2016, **18**, 3066.
37 J.-P. Tessonnier, M. Becker, W. Xia, F. Girgsdies, R. Blume, L. Yao, D. S. Su, M. Muhler and R. Schlögl, *ChemCatChem*, 2010, **2**, 1559.
38 L. Zhang, Z. Su, F. Jiang, L. Yang, J. Qian, Y. Zhou, W. Li and M. Hong, *Nanoscale*, 2014, **6**, 6590.
39 Y. Xiao, P. P. Sun and M. H. Cao, *ACS Nano*, 2014, **8**, 7846.
40 Y. Xiao, M. Cao, L. Ren and C. Hu, *Nanoscale*, 2012, **4**, 7469.
41 N. Mahmood, C. Z. Zhang, F. Liu, J. H Zhu and Y. L. Hou, *ACS Nano*, 2013, **7**, 10307.
42 Y. Hwa, J. H. Sung, B. Wang, C.-M. Park and H.-J. Sohna, *J. Mater. Chem.*, 2012, **22**, 12767.
43 J. M. Li, Y. Fu, X. D. Shi, Z. M. Xu and Z. A. Zhang, *Chem.–Eur. J.*, 2016, **22**, DOI: 10.1002/chem.201604532.
44 Z. H. Wang, X. Q. Xiong, L. Qie and Y. H. Huang, *Electrochim. Acta*, 2013, **106**, 320.
45 L. Chen, Z. Y. Wang, C. N. He, N. Q. Zhao, C. S. Shi, E. Z. Liu and J. J. Li, *ACS Appl. Mater. Interfaces*, 2013, **5**, 9537.
46 J. Zhang, Z. X. Yang, J. C. Qiu and H. W. Lee, *J. Mater. Chem. A*, 2016, **4**, 5802.
47 J. Park, S. Kim, O. Park and J. M. KO, *Appl. Phys. A*, 2006, **82**, 593.